

SingLEM: Single-Channel Large EEG Model

Jamiyan Sukhbaatar, Satoshi Imamura, Ibuki Inoue, Shoya Murakami, Kazi Mahmudul Hassan, Seungwoo Han, Ingon Chanpornpakdi, and Toshihisa Tanaka

Abstract—Current deep learning models for electroencephalography (EEG) are often task-specific and depend on large labeled datasets, limiting their adaptability. Although emerging foundation models aim for broader applicability, their rigid dependence on fixed, high-density multi-channel montages restricts their use across heterogeneous datasets and in missing-channel or practical low-channel settings. To address these limitations, we introduce SingLEM, a self-supervised foundation model that learns robust, general-purpose representations from single-channel EEG, making it inherently hardware agnostic. The model employs a hybrid encoder architecture that combines convolutional layers to extract local features with a hierarchical transformer to model both short- and long-range temporal dependencies. SingLEM is pretrained on 71 public datasets comprising over 9,200 subjects and 357,000 single-channel hours of EEG. When evaluated as a fixed feature extractor across six motor imagery and cognitive tasks, aggregated single-channel representations consistently outperformed leading multi-channel foundation models and hand-crafted baselines. These results demonstrate that a single-channel approach can achieve state-of-the-art generalization while enabling fine-grained neurophysiological analysis and enhancing interpretability. The source code and pretrained models are available at <https://github.com/ttlabtua/SingLEM>.

Index Terms—Electroencephalography, foundation models, single-channel

I. INTRODUCTION

LECTROENCEPHALOGRAPHY (EEG) is a non-invasive neurophysiological technique that measures brain activity through scalp electrodes. Because of its high temporal resolution, portability, and affordability, EEG is widely applied in diverse domains, including brain-computer interfaces (BCIs) [1], sleep staging [2], seizure detection [3], [4], [5], clinical diagnosis [6], [7], and emotion recognition [8], [9], [10]. Despite its potential, EEG analysis is challenged by non-stationarity across subjects and sessions, susceptibility to noise (e.g., ocular or muscular artifacts), and low signal-to-noise ratios [11]. To address this, deep neural networks (DNNs) have emerged as the state-of-the-art paradigm, learning complex and task-relevant features automatically from raw data [12].

This work was supported in part by JSPS KAKENHI 23H00548. The work of Jamiyan Sukhbaatar was supported by the Mongolia-Japan Engineering for Education Development (MJEED) project. (Corresponding author: Toshihisa Tanaka.)

Jamiyan Sukhbaatar is with the Department of Electronic and Information Engineering, Tokyo University of Agriculture and Technology, Koganei-Shi 184-8588, Japan, and also with the Department of Electronics and Communication Engineering, National University of Mongolia, Ulaanbaatar, 14200 Mongolia (e-mail: jamiyan@sip.tuat.ac.jp).

Satoshi Imamura, Ibuki Inoue, Shoya Murakami, Kazi Mahmudul Hassan, Seungwoo Han, Ingon Chanpornpakdi, and Toshihisa Tanaka are with the Department of Electronic and Information Engineering, Tokyo University of Agriculture and Technology, Koganei-Shi 184-8588, Japan. (e-mail: tanakat@cc.tuat.ac.jp)

While DNNs have achieved remarkable success in various EEG decoding tasks, including motor imagery (MI) classification [13], [14], SSVEP decoding [15], [16], sleep stage classification [17], [18], and cognitive workload estimation [19], [20], this task-specific end-to-end paradigm suffers from the following limitations. First, these models are not generalizable and must be retrained for each new task. Second, they require substantial labeled data, which is costly and time-consuming to acquire. Third, the high inter-subject and inter-session variability inherent in EEG signals makes it difficult for these models to generalize to new users. These challenges highlight the urgent need for scalable, data-efficient, and generalizable EEG representation learning.

Inspired by the success of foundation models in natural language processing [21], [22] and computer vision [23], recent studies have proposed foundation models for biomedical engineering and healthcare [24], [25], [26]. Such models leverage large-scale self-supervised pretraining to extract generalizable representations, which can be transferred to multiple downstream tasks with minimal fine-tuning. Their adaptability makes foundation models an attractive solution to the challenges of data scarcity and inherent signal variability in EEG analysis.

As a result, several EEG-specific foundation models have emerged, including BENDR [27], BIOT [28], LaBraM [29], and CBraMod [30]. A critical limitation of these pioneering works is that their architectures are often rigidly tied to fixed high-density electrode montages, limiting their utility in rehabilitation and assistive BCI scenarios where hardware diversity and low-channel configurations are the norm. Although adaptation through fine-tuning is possible, it is a resource-intensive process that undermines the goal of having a universal, data-efficient model. Consequently, their direct application is hindered by their inability to adapt to different electrode layouts and missing channel data.

To overcome this challenge, instead of forcing a model to operate directly on multi-channel signals, we take a fundamentally different approach. EEG waveforms are montage dependent, and therefore, approaches that directly model multi-channel data introduce architectural rigidity and limit generalization. In contrast, our approach learns robust representations at the single-electrode level and applies late fusion to integrate them for downstream tasks. This design makes the model naturally montage independent and well-suited for scenarios with heterogeneous or low-channel configurations.

Building on this motivation, we propose SingLEM, a self-supervised foundation model that learns EEG representations at the single-channel level. SingLEM is built on an asymmetric masked autoencoder (MAE) backbone [31] that integrates convolutional layers for local feature extraction with a hierarchical

transformer to capture both short- and long-range temporal dependencies.

We pretrained SingLEM on 71 public EEG datasets encompassing over 10,200 hours of multi-channel recordings (equivalent to 357,000 hours of single-channel data). This training on large-scale data enables robust channel-level representation learning to facilitate deployment across diverse montages, including single-electrode settings. These representations can be used individually or combined for downstream classification with lightweight classifiers (e.g., SVMs) without task-specific fine-tuning. Although spatial dependencies are not explicitly modeled during pretraining, spatial patterns can be recovered post hoc by aggregating per-channel representations. Hence, SingLEM provides a general-purpose EEG representation framework that is robust to inter-subject variability, montage differences, and data scarcity.

The main contributions of this study are summarized as follows:

- We introduce SingLEM, a self-supervised foundation model that learns general-purpose representations from single-channel EEG, making it inherently hardware-agnostic and adaptable across diverse montages.
- We demonstrate that concatenated single-channel representations from SingLEM consistently outperform state-of-the-art multi-channel foundation models across six diverse EEG tasks.
- We establish SingLEM as an efficient frozen feature extractor, substantially reducing computational costs while maintaining high downstream performance.
- SingLEM is pretrained on 71 diverse datasets, totaling over 357,000 single-channel hours of recordings from more than 9,200 subjects.

II. RELATED WORK

A. Task-Specific Deep Learning for EEG Decoding

Early deep learning approaches for EEG focused on end-to-end architectures trained from scratch on labeled data for individual tasks (e.g., MI classification). While effective, this paradigm requires a new model to be trained for new tasks. These models can be categorized into two groups: convolutional neural networks (CNNs) and transformers.

CNN-based models have proven highly effective at capturing local spatiotemporal features from EEG signals. DeepConvNet and ShallowConvNet [32] introduced direct raw-EEG processing via 5-layer and 2-layer CNNs, respectively. EEGNet [33] further advanced this line of investigation using depthwise and separable convolutions to achieve lightweight yet effective feature extraction. SPaRCNet [34] employs 1D-CNNs with dense residual connections for seizure detection. While CNNs excel at local temporal–spatial feature learning, their limited receptive fields limit the modeling of long-range dependencies.

Transformer-based models leverage self-attention to understand the global context. In the EEG domain, EEG-Conformer [35] was designed to effectively capture both local, fine-grained features via its convolutional module and global, long-range dependencies through its self-attention mechanism.

SSVEPformer [16] is specifically designed for the classification of steady state visual evoked potentials (SSVEPs). EEG-Deformer [36] introduced a hierarchical transformer to capture both coarse and fine temporal dynamics in the EEG signals. These models have achieved state-of-the-art performance on various tasks.

However, a fundamental limitation unites these end-to-end approaches: they require a large amount of labeled data for training, which cannot be easily transferred across tasks or montages. This has motivated a shift towards more generalizable, pretrained models.

B. Self-Supervised Learning and Foundation Models for EEG

To overcome the limitations caused by task specificity and data scarcity, recent research has turned to self-supervised learning to pretrain large foundation models on a vast amount of unlabeled EEG data. The goal is to learn universal representations of EEG signals that can be transferred to various downstream tasks with minimal fine-tuning. Two main paradigms have emerged:

Contrastive learning (e.g., BENDR [27] and BIOT [28]) generates discriminative EEG representations by enforcing closeness between similar EEG segments (positive pairs) and maximizing distance from dissimilar segments (negative pairs) within the learned embedding space. The challenge lies in the selection and construction of appropriate positive and negative pairs.

Generative (masked) learning, inspired by the success of BERT [21] and MAE [31], has become a prominent self-supervised learning paradigm for EEG. In this approach, a portion of the input EEG signal is intentionally masked, and the model is trained to reconstruct the masked data based on the unmasked context. This process enables the model to acquire rich, contextualized representations. The benchmark foundation models in this study, LaBraM [29] and CBraMod [30], primarily adopt this approach. Specifically, LaBraM employs patch-based predictive coding, whereas CBraMod employs criss-cross attention to model inter-channel relations.

C. Research Gap: Limited Adaptability of Existing Multi-Channel EEG Foundation Models

The research reviewed above offers a promising path for developing general-purpose EEG foundation models. However, their practical utility as fixed, “ready-to-use” feature extractors is significantly limited by two core issues: rigid architectural assumptions regarding channel configurations and limited diversity in their pretraining corpora.

First, existing models are tightly coupled to the channel layouts used during pretraining. For example, BENDR [27] is restricted to exactly 19 channels—the same configuration as its pretraining dataset—making it unusable for datasets with different electrode counts. BIOT [28], while nominally more flexible, is pretrained on a fixed set of 16 bipolar and 2 monopolar channels; mismatches in downstream tasks can degrade performance. LaBraM [29] uses learnable absolute positional embeddings tied to specific electrode labels, which assumes fixed spatial and reference properties. This

restricts its ability to generalize to unseen montages containing novel electrode labels. Similarly, CBraMod [30], although it incorporates a more flexible positional encoding strategy, remains pretrained on a fixed 19-channel setup. This common characteristic of tight coupling in the architecture creates the following significant barriers for direct, feature-extraction use:

- Montage inflexibility: These models cannot be readily deployed across datasets with different montages (e.g., 10–20 or bipolar) or varying numbers of electrodes without computationally intensive retraining or fine-tuning.
- Poor robustness to incomplete or reordered data: Their performance degrades significantly if channels expected by the model are missing or reordered, a common occurrence in real-world data collection.
- Unsuitability for low-channel applications: They are incompatible with the many clinical, consumer, and BCI applications that rely on few-channel or even single-channel EEG recordings because of cost, comfort, and setup time.

Second, the generalizability of foundation models is constrained by the narrow scope of their pretraining corpora. For instance, BIOT [28] was pretrained on six public EEG datasets, while BENDR [27] and CBraMod [30] primarily rely on the Temple University Hospital EEG Corpus, which comprises clinical data from a single institutional setting. Similarly, LaBraM [29] was pretrained on a smaller collection of around twenty public datasets. Such corpora lack the diversity of recording conditions, tasks, and populations needed for broad generalization. As a result, pretrained representations may capture dataset-specific biases rather than universal EEG features, leading to degraded performance when transferred across hardware, paradigms, or subject groups.

In summary, these limitations restrict the practical value of existing EEG foundation models. In scenarios where a pretrained model is expected to function as a fixed, universal feature extractor without computationally expensive fine-tuning, rigid montage assumptions and limited pretraining diversity emerge as critical bottlenecks. This motivates the need for a new approach that is inherently montage-agnostic, capable of operating across heterogeneous datasets, and trained on a sufficiently large and diverse corpus to ensure robust generalization.

To address this gap, we propose SingLEM, a montage-agnostic foundation model that learns EEG representations at the single-channel level, inherently decoupling representation learning from electrode layouts. By pretraining on one of the most diverse EEG corpora to date (71 datasets, 357,000+ single-channel hours, 9,200+ subjects), SingLEM achieves both adaptability to different montages and large-scale generalizability, making it suitable for practical deployment across research, clinical, and consumer applications.

III. METHOD

This section outlines the proposed model architecture, data preprocessing, tokenization, formulation of the model, training procedure, and implementation details.

A. Overview

SingLEM is a self-supervised model for learning context-rich, robust representations from single-channel EEG signals without requiring fine-tuning for downstream tasks. SingLEM, as shown in Fig. 1, adopts an asymmetric MAE framework, employing a lightweight decoder and token masking applied solely during pretraining. The asymmetric design ensures that the encoder, rather than the decoder, is responsible for reconstructing the masked signals. By limiting the decoder’s capacity, the model avoids the latent collapse and forces the encoder to capture informative and discriminative EEG features in its latent space. The encoder, trained to extract low-dimensional latent representations, is composed of three sequential modules: the temporal encoder, feature embedding module, and global transformer encoder. The lightweight CNN-based temporal encoder is introduced to capture frequency-specific features. The feature embedding module captures local temporal context, while the global transformer encoder integrates long-range dependencies across the EEG sequence.

B. Data Collection and Preprocessing

A large corpus of multi-channel EEG recordings was collected from the publicly available datasets listed in Table I. Each dataset differs with respect to sampling rate, file format, montage, recording duration, subject cohort, and acquisition device. To unify datasets while preserving raw signal characteristics, we applied the following minimal preprocessing:

- 1) Band-pass filtering (0.5–50 Hz): zero-phase FIR filtering to remove drift and high-frequency noise.
- 2) Notch filtering: to attenuate powerline interference.
- 3) Resampling to 128 Hz: to standardize temporal resolution across datasets.
- 4) Artifact rejection: any sample that exceeds $\pm 100\mu V$ is discarded.
- 5) Scaling: all data are multiplied by 10^4 so that amplitudes fall within the range (-1, 1).

Following preprocessing, each channel’s waveform is transformed into a continuous 1D EEG signal with uniform sampling and a bounded amplitude.

C. EEG Tokenization

To facilitate transformer-based processing, continuous, preprocessed EEG signals are segmented into fixed-length overlapping tokens. This ensures a consistent input format for the transformer while preserving temporal context. Let the preprocessed signal be $\mathbf{X} \in \mathbb{R}^{1 \times S}$, where S is the total number of samples at 128 Hz. We define each token to cover $\ell = 128$ samples (1 s), with an overlap of $u = 32$ samples (250 ms) [37] between successive tokens. Consequently, the stride is $s = \ell - u = 96$. The number of tokens is $L = \lfloor (S - \ell)/s \rfloor + 1$, and for $i = 0, \dots, L - 1$, the i -th token \mathbf{T}_i is extracted as

$$\mathbf{T}_i = \mathbf{X}[i s : i s + \ell - 1] \in \mathbb{R}^{1 \times \ell}. \quad (1)$$

This overlapping scheme ensures each pair of adjacent tokens contains exactly $u = 32$ identical samples, thereby capturing transient events at the segment boundaries [37].

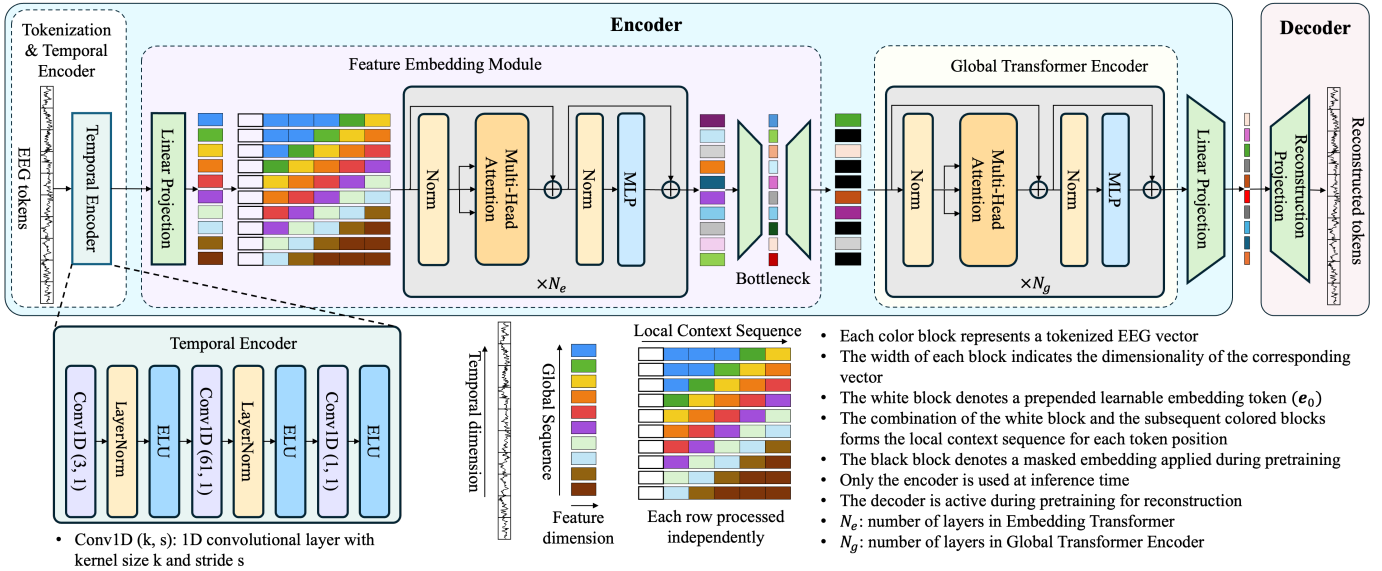


Fig. 1. Architecture of SingLEM. The model comprises three main modules: the temporal encoder, the feature embedding module, and the global transformer encoder. The temporal encoder extracts band-specific features from each EEG token independently. The feature embedding module enriches tokens with short-term contextual information using a sliding window mechanism. The global transformer encoder then integrates long-range dependencies across the sequence, yielding robust and context-aware representations.

Finally, we append a special end-of-channel (EOC) token after the last token of each channel to prevent unintended mixing when concatenating multiple channels or recordings.

D. Encoder Architecture

The encoder is composed of three sequential modules, each designed to progressively capture and encode distinct levels of temporal abstraction from the input EEG signals. These three modules (the temporal encoder, feature embedding, and global transformer encoder modules) jointly learn hierarchical representations that reflect local spectral content, short-term contextual dependencies, and global sequence-level dynamics, respectively.

Temporal Encoder: Each EEG token T_i is processed independently through a three-layer 1D CNN to extract band-specific temporal features, emulating band-pass filtering operations that span standard EEG frequency bands, from delta (0.5–4 Hz) to gamma (30–50 Hz). Each convolution layer is followed by normalization (LN) and ELU activation to stabilize optimization and introduce nonlinearity. The first layer ($K^{(1)}=3$) captures high-frequency details, particularly in the gamma range. The second layer ($K^{(2)}=61$) targets slow oscillatory components, including delta activity. The final layer ($K^{(3)}=1$) acts as a channel-wise projection that consolidates features across filters while preserving the temporal length (ℓ), producing per-token feature vectors for downstream embedding.

Let $\text{Conv}^{(k)}$ denote the k -th convolution layer, and define $\mathbf{U}_i^{(0)} = \mathbf{T}_i \in \mathbb{R}^{1 \times \ell}$. The processing can be expressed as

$$\mathbf{U}_i^{(k)} = \begin{cases} \text{ELU}(\text{LN}(\text{Conv}^{(k)}(\mathbf{U}_i^{(k-1)}))), & k = 1, 2, \\ \text{ELU}(\text{Conv}^{(3)}(\mathbf{U}_i^{(2)})), & k = 3, \end{cases} \quad (2)$$

where $\mathbf{U}_i^{(3)} \in \mathbb{R}^{1 \times \ell}$ serves as the initial token-level representation and is passed to the feature embedding module for contextualization.

Feature Embedding Module: After token-level features have been extracted, a dedicated feature embedding module is applied to capture short-range temporal dependencies. This module produces contextualized embeddings for each token by integrating information from its temporal neighbors through a sliding window mechanism.

As the initial step, token-level features $\{\mathbf{U}_i^{(3)}\}$ are linearly projected from the CNN feature space into a learnable embedding space of dimension d via $\mathbf{W}_E \in \mathbb{R}^{\ell \times d}$, which serves as an interface between the temporal encoder and subsequent transformer layers, expressed as

$$\mathbf{V}_i = \mathbf{U}_i^{(3)} \mathbf{W}_E. \quad (3)$$

This projection yields a sequence of embedded tokens $\{\mathbf{V}_i\}_{i=1}^L$, where each $\mathbf{V}_i \in \mathbb{R}^{1 \times d}$. For each token position i , we construct a local context window of width w centered on \mathbf{V}_i using boundary replication for edge padding, as follows

$$\mathbf{S}_i = [\mathbf{V}_{i-\lfloor w/2 \rfloor}, \dots, \mathbf{V}_{i+\lfloor w/2 \rfloor}] \in \mathbb{R}^{w \times d}. \quad (4)$$

For each local context window \mathbf{S}_i , we prepend a learnable embedding token $\mathbf{e}_0 \in \mathbb{R}^d$ to form the local context sequence, as follows:

$$\tilde{\mathbf{S}}_i = [\mathbf{e}_0; \mathbf{S}_i] \in \mathbb{R}^{(w+1) \times d}. \quad (5)$$

To preserve temporal order, a positional embedding matrix $\mathbf{P} \in \mathbb{R}^{(w+1) \times d}$ is added element-wise, as follows:

$$\mathbf{H}_i = \tilde{\mathbf{S}}_i + \mathbf{P}. \quad (6)$$

Each local context sequence \mathbf{H}_i is independently processed by a lightweight transformer with N_e layers. Unlike typical global transformers, our design ensures that each \mathbf{H}_i models

only local context. We implement this by reshaping the input batch as $(\text{batch_size} \times L)$, allowing all L local windows to be processed in parallel. This design prioritizes the efficient modeling of local dependencies before global integration.

Each transformer layer contains a multi-head self-attention (MHSA) block and a feed-forward network (FFN), both wrapped with residual connections and layer normalization as follows

$$\mathbf{A}_i = \text{MHSA}(\text{LN}(\mathbf{H}_i)) + \mathbf{H}_i, \quad (7)$$

$$\mathbf{Z}_i = \text{FFN}(\text{LN}(\mathbf{A}_i)) + \mathbf{A}_i. \quad (8)$$

The FFN comprises two linear layers with an intermediate GELU activation, projecting the dimension as $d \rightarrow 4d \rightarrow d$.

After N_e layers, the output corresponding to the prepended token (index 0) is selected as the contextual embedding $\mathbf{z}_i \in \mathbb{R}^d$. This embedding is then passed through an MLP-based bottleneck as

$$\mathbf{e}_i = \mathbf{W}_{b3} \text{GELU}(\mathbf{W}_{b2} \text{GELU}(\mathbf{z}_i \mathbf{W}_{b1} + \mathbf{b}_1) + \mathbf{b}_2) + \mathbf{b}_3, \quad (9)$$

where $\mathbf{W}_{b1} \in \mathbb{R}^{d \times \frac{d}{2}}$, $\mathbf{W}_{b2} \in \mathbb{R}^{\frac{d}{2} \times d_{\text{emb}}}$, $\mathbf{W}_{b3} \in \mathbb{R}^{d_{\text{emb}} \times d}$, and $d_{\text{emb}} < d$. This bottleneck encourages the representation to retain only the most salient features from each local context window, producing compact and highly informative embeddings.

Global Transformer Encoder: To model long-range temporal dependencies across the entire EEG sequence, the contextualized embeddings $\{\mathbf{e}_i\}_{i=1}^L$ are stacked into $\mathbf{E} = [\mathbf{e}_1; \dots; \mathbf{e}_L] \in \mathbb{R}^{L \times D}$, and augmented with learnable positional embeddings $\mathbf{Q} \in \mathbb{R}^{L \times D}$ as follows:

$$\mathbf{G}^{(0)} = \mathbf{E} + \mathbf{Q}. \quad (10)$$

This sequence $\mathbf{G}^{(0)}$ is processed by a transformer encoder with N_g layers, each comprising an MHSA block followed by an FFN, both with pre-layer normalization and residual connections. Unlike the feature embedding module, no MLP bottleneck is applied, and the attention is computed globally across all tokens.

After the final layer, the outputs $\mathbf{G}^{(N_g)} \in \mathbb{R}^{L \times D}$ are projected via $\mathbf{W}_R \in \mathbb{R}^{D \times r}$ to produce the following final per-token representations:

$$\mathbf{R} = \mathbf{G}^{(N_g)} \mathbf{W}_R. \quad (11)$$

These per-token representations $\mathbf{R} \in \mathbb{R}^{L \times r}$ serve as the latent features used for downstream tasks such as classification or regression.

This hierarchical design—processing from local temporal filtering, to short-term contextualization, and finally to global integration—is designed to capture multi-scale dependencies within the EEG token sequences.

E. Pretraining SingLEM

We employ a self-supervised MAE paradigm when pre-training SingLEM. Each pretraining batch comprises randomly sampled sequences of consecutive EEG tokens extracted from the preprocessed data. The presence of the EOC tokens ensures

that token sequences remain within the same EEG channel. Although sequence lengths can vary across batches, each batch has a uniform length for computational consistency.

The pretraining pipeline consists of the following stages:

Masking: From the feature embedding module, we obtain per-token contextual embeddings $\mathbf{E} = [\mathbf{e}_1; \dots; \mathbf{e}_L] \in \mathbb{R}^{L \times D}$. A fixed proportion $p = 0.5$ of these token embeddings is randomly selected for masking. Let $\mathcal{M} \subset \{1, \dots, L\}$ denote the set of masked indices. The masked sequence is then

$$\tilde{\mathbf{e}}_i = \begin{cases} \mathbf{0}, & i \in \mathcal{M} \\ \mathbf{e}_i, & \text{otherwise,} \end{cases} \quad (12)$$

yielding $\tilde{\mathbf{E}} = [\tilde{\mathbf{e}}_1, \dots, \tilde{\mathbf{e}}_L] \in \mathbb{R}^{L \times D}$.

Global transformer encoding and projection: To encode sequence order, learnable positional embeddings $\mathbf{Q} \in \mathbb{R}^{L \times D}$ are added using $\mathbf{G}^{(0)} = \tilde{\mathbf{E}} + \mathbf{Q}$. The result is then processed by the global transformer encoder, and its final outputs $\mathbf{G}^{(N_g)}$ are linearly projected to the encoder’s final representations $\mathbf{R} = [\mathbf{r}_1; \dots; \mathbf{r}_L] \in \mathbb{R}^{L \times r}$.

Reconstruction: Each representation \mathbf{r}_i is mapped back to the original token space using a shared lightweight decoder as follows:

$$\hat{\mathbf{T}}_i = \mathbf{r}_i \mathbf{W}_{\text{dec}} + \mathbf{b}_{\text{dec}}, \quad \mathbf{W}_{\text{dec}} \in \mathbb{R}^{r \times \ell}, \quad \hat{\mathbf{T}}_i \in \mathbb{R}^{1 \times \ell}. \quad (13)$$

Unlike conventional MAE approaches [21], [31], which reconstruct only the masked tokens, we jointly minimize the reconstruction loss over both masked and unmasked tokens. This ensures that the encoder’s compressed representations preserve all the information for downstream use.

Loss computation: We optimize the following three loss terms:

$$\mathcal{L}_{\text{masked}} = \frac{1}{|\mathcal{M}|} \sum_{i \in \mathcal{M}} \text{Huber}(\mathbf{T}_i, \hat{\mathbf{T}}_i), \quad (14)$$

$$\mathcal{L}_{\text{unmasked}} = \frac{1}{L - |\mathcal{M}|} \sum_{i \notin \mathcal{M}} \text{Huber}(\mathbf{T}_i, \hat{\mathbf{T}}_i), \quad (15)$$

$$\mathcal{L}_{\beta\gamma} = \frac{1}{L} \sum_{i=1}^L \left\| \text{BP}_{13-50}(\mathbf{T}_i) - \text{BP}_{13-50}(\hat{\mathbf{T}}_i) \right\|_2^2, \quad (16)$$

where $\text{Huber}(\cdot)$ denotes the Huber loss function and $\text{BP}_{13-50}(\cdot)$ denotes a zero-phase filter retaining frequencies in the 13–50 Hz range. The total pretraining loss is

$$\mathcal{L} = \lambda_1 \mathcal{L}_{\text{masked}} + \lambda_2 \mathcal{L}_{\text{unmasked}} + \lambda_3 \mathcal{L}_{\beta\gamma}, \quad (17)$$

with λ_1 , λ_2 , and λ_3 controlling the contribution of each term.

After convergence, the decoder and mask module are discarded, and the final encoder can now be used as a feature extractor for downstream tasks.

F. Implementation Details

The CNN-based temporal encoder consisted of three convolutional layers, $\text{Conv}^{(1)}$, $\text{Conv}^{(2)}$, and $\text{Conv}^{(3)}$, with output channels set to 32, 32, and 1, respectively. The feature vectors from the temporal encoder were individually projected into a $d = 128$ dimensional space. For local contextualization, a

TABLE I
SUMMARY OF THE 71 PUBLIC EEG DATASETS USED IN THIS STUDY

Dataset (Year)	Ref.	Task / Type	Subj.	Ch.	Rate [Hz]	Duration [h]	Format
Cho (2017)	[38]	MI	52	64	512	244.80	MAT
Schalk (2009)	[39]	MI	109	64	160	49.00	EDF
Shin (2016)	[40]	MI	29	30	200	29.00	MAT
Kaya (2017)	[41]	MI	13	22	1000	67.60	MAT
Lee (2019)	[42]	MI+ERP+SSVEP	54	62	1000	255.10	MAT
Brandl (2020)	[43]	Cognitive: Stroop	16	63	1000	19.75	MAT
Chen (2023)	[44]	Visual: Color-Word	21	34	1000	1.32	Neuroscan
Mou (2024)	[45]	Cognitive	608	64	1000	166.16	EDF
Getzmann (2024)	[46]	Cognitive	10	128	1000	118.85	BrainVision
Ji (2024)	[47]	Cognitive	80	64	1000	186.16	MAT
Momenian (2024)	[48]	Auditory: Story	52	64	1000	18.95	EEGLAB
Xiang (2024)	[49]	Sleep	71	61	500	17.75	EEGLAB
Babayan (2021)	[50]	Sleep	2,274	62	500	60.17	BrainVision
van Dijk (2022)	[51]	ERP	1,274	22	2500	88.86	BrainVision
Ngo (2022)	[52]	Cognitive: Spelling	178	34	1000	66.32	EDF
Grootswagers (2022)	[53]	Visual: RSVP	50	128	1000	41.73	BrainVision
Dzianok (2024)	[54]	Memory	79	128	1000	44.51	BrainVision
Ma (2022)	[55]	MI	25	32	250	12.99	MAT
Chen (2019)	[56]	Cognitive: Deception	24	31	500	64.72	BrainVision
Cao (2024)	[57]	Cognitive: Sustained	27	32	500	81.94	EEGLAB
Telesford (2023)	[58]	Visual: Movie	22	64	5000	5.90	EEGLAB
Ma (2020)	[59]	MI	25	64	500	45.41	Neuroscan
Yang (2025)	[60]	MI	62	64	1000	127.83	Biosemi
Chen (2022)	[61]	Cognitive	31	128	1000	40.10	EEGLAB
Dreyer (2022)	[62]	MI	87	27	512	71.78	GDF
Wang (2023)	[63]	Memory	60	63/64	500	74.98	BrainVision
Chen (2023)	[64]	Emotion Recognition	123	32	1000	155.28	Biosemi
Shin (2018)	[65]	Cognitive	26	28	1000	40.19	BrainVision
Hinss (2023)	[66]	Cognitive: Vigilance	29	64	500	81.04	EEGLAB
Gebodh (2022)	[67]	Cognitive: Vigilance	26	32	1000	72.78	EEGLAB
Nieto (2022)	[68]	Inner Speech	10	128	1024	12.95	Biosemi
Won (2018)	[69]	P300	55	32	512	44.09	EEGLAB
Hollenstein (2022)	[70]	Reading	30	128	500	43.13	MAT
Liu (2019)	[71]	MI	27	64	1000	33.45	EEGLAB
Wagner (2025)	[72]	Motor: Walking	20	108	512	39.84	EEGLAB
Ghosh (2019)	[73]	Cognitive: Stroop	40	32	128	3.30	MAT
Valdes-Sosa (2021)	[74]	Clinical Activation Protocol	282	64/120	200	107.90	EDF
Mheich (2021)	[75]	Cognitive	43	256	1000	24.74	BrainVision
Liu (2024)	[76]	MI	50	29	500	4.44	EDF
Choi (2024)	[77]	Emotion (Voice)	44	63	1000	46.55	MAT
Wei (2024)	[78]	Sleep	29	19	1000	217.78	EDF
Gu (2024)	[79]	SSVEP	30	64	1000	235.78	EDF
Mumtaz (2017)	[80]	ERP: Oddball	64	19	256	4.44	MAT
Iwama (2023)	[81]	Sensorimotor Rhythm	138	128	1000	154.28	EDF
Liwicki (2023)	[82]	Inner Speech	4	64	512	1.47	Biosemi
Moffa (2022)	[83]	Brain Stimulation	24	64	2048	125.58	MAT
Cuevas-Romero (2022)	[84]	Auditory: Tinnitus	89	17	256	99.17	EEGLAB
Pei (2022)	[85]	Cognitive: Alertness	74	64	1000	110.16	Curry
Lin (2025)	[86]	Epilepsy (IED)	52	19	500	28.00	MAT
Pavlov (2022)	[87]	Cognitive: Memory	65	64	1000	140.73	EEGLAB
Liu (2022)	[88]	SSVEP	100	64	1000	19.68	EDF
Cai (2022)	[89]	Visual: Faces	53	128/3	250	16.57	MAT/RAW
Pascucci (2022)	[90]	Visual: Face ID	20	128	2048	10.57	Biosemi
Stieger (2021)	[91]	MI	62	64	1000	613.34	MAT
Lopez (2015)	[92]	Abnormal	2,383	Varies	250	1,141.00	EDF
Buckwalter (2021)	[93]	Artifact	213	Varies	250	99.98	EDF
Veloso (2017)	[94]	Epilepsy	200	Varies	250	631.84	EDF
Harati (2015)	[95]	Event	370	Varies	250	129.49	EDF
Shah (2018)	[96]	Seizure	675	Varies	250	1,473.57	EDF
von Weltin (2017)	[97]	Slowing	38	Varies	250	27.60	EDF
Grootswagers (2025)	[98]	Visual Perception	42	32	500	5.52	EEGLAB
Yi (2025)	[99]	MI	18	64	1000	32.48	Neuroscan
Rybář (2025)	[100]	Mental Task	19	64	2048	22.29	Biosemi
He (2025)	[101]	Visual: Object ID	40	32	500	23.73	EDF
Xue (2025)	[102]	Visual: RSVP	32	64	1000	157.93	Curry
Bai (2025)	[103]	Reading	30	64	1000	12.92	Biosemi
Moreira (2025)	[104]	Speech Decoding	24	64	1000	50.76	EDF
Wang (2024)	[105]	Auditory: Listening	26	64	500	19.20	BrainVision
Zhang (2025)	[106]	Object Viewing	35	64	500	23.70	EEGLAB
Tao (2024)	[107]	Driving Task	35	59	1000	55.07	Biosemi
López-Larraz (2025)	[108]	Sleep	128	2/6	256	2,002.59	EDF

temporal window of $w = 5$ within the contextual embedding module was used. The feature embedding transformer consisted of $N_e = 4$ layers with four attention heads each. The subsequent MLP bottleneck projected the token embeddings to $d_{\text{emb}} = 32$. The global transformer encoder was implemented with $D = 128$, $N_g = 12$ layers, and eight attention heads per layer. A final linear projection of each token resulted in an output with a compact representation of size $r = 16$.

The SingLEM was implemented in PyTorch and trained for 16 epochs on four NVIDIA A100 GPUs using distributed data parallelism. The optimizer was AdamW ($\beta_1 = 0.9$, $\beta_2 = 0.95$, and a weight decay of 10^{-1}) with a cosine annealing learning rate schedule that decayed from 10^{-4} to 10^{-6} , and a batch size of 1024.

IV. EXPERIMENTS

This section outlines the experimental framework for evaluating the proposed SingLEM model. It includes baseline models, datasets, a preprocessing pipeline, an evaluation protocol, implementation details, and performance metrics.

A. Baselines

We benchmarked SingLEM with four pretrained EEG foundation models and traditional baselines that use handcrafted frequency-domain features.

1) *Foundation Models*: We compared SingLEM with BENDR [27], BIOT [28], LaBraM [29], and CBraMod [30]. A major challenge in utilizing these models is their dependency on a fixed channel montage. BIOT was pretrained on 16 bipolar and two monopolar channels, whereas CBraMod was pretrained on 19 specific channels from the 10–20 montage. BENDR was also pretrained on 19 standard EEG channels but required the addition of a 20th channel containing a constant value derived from the signal’s amplitude scaling factor. For fair comparison, we selected the exact channels required by each pretrained model. When a required channel was missing in a downstream dataset, we substituted it with the physically closest available electrode. If no suitable substitute existed, the model was evaluated without that channel, and the potential mismatch is acknowledged.

2) *Frequency-Domain Features*: To benchmark the proposed model against a robust non-deep-learning approach, we extracted handcrafted features using the fast Fourier transform (FFT). For each EEG trial, we selected the top- k complex-valued Fourier coefficients (ranked by magnitude) from the real-valued FFT (rFFT). The magnitudes and corresponding phases of the selected coefficients were then concatenated into a $2k$ -dimensional feature vector for each channel. We evaluated two configurations: $k = 8$ and $k = 16$ coefficients per second of EEG data to assess performance with different feature dimensionalities.

B. Datasets and Preprocessing

1) *Datasets*: We evaluated SingLEM on six diverse EEG classification tasks: three MI and three cognitive tasks, derived from three publicly available EEG datasets.

MI Datasets: a) **Dreyer-MI-2C** [62]: This dataset contains two-class MI (left vs. right hand) recordings. The original publication provides three subsets (A, B, and C). To reduce computational overhead, we utilized Dataset B for this study, which contains data from 21 participants. EEG data was recorded using a g.USBamp (g.tec, Austria) amplifier from 27 active electrodes placed according to the international 10–20 system and a sampling rate of 512 Hz. Each subject completed six runs, of which the last four runs were designated for user training. Each trial lasted 8 s, initiated by a visual cue at $t = 3$ s. Following standard BCI protocol, we extracted the 5-s segment from $t = 3$ s to $t = 8$ s corresponding to the active MI period. We utilized data from the four user-training runs, yielding 160 trials per subject. b) **WBCIC-MI-2C** [60]: This large-scale two-class MI dataset (left- vs. right-hand grasping) was collected from 51 healthy subjects during the 2019 World Robot Conference Contest-BCI Robot Contest MI (WBCIC-MI). Data were recorded with a 64-channel wireless EEG system (Neuracle, China) using 59 EEG channels (10–20 montage) at 1,000 Hz. Each 7.5-second trial included a 4-s MI period. We used all 200 trials from the first recording session for each subject. c) **WBCIC-MI-3C** [60]: This dataset is also from the WBCIC-MI collection, and it contains three-class MI (left-hand grasping, right-hand grasping, and foot hooking) recordings from 11 healthy subjects. The recording setup and trial structure were identical to those of the WBCIC-MI-2C. We used all 300 trials from the first session for each subject.

Cognitive Task Datasets: The following three datasets were obtained from a study on simultaneous EEG-NIRS acquisition during cognitive tasks [65]. Data for all three tasks was acquired from 26 healthy participants using a BrainAmp amplifier (Brain Products GmbH, Germany). EEG was recorded from 30 electrodes (10–5 montage), with two used for reference and ground, yielding 28 channels for analysis. For all tasks, we extracted 10-s trials. a) **N-back-2C**: This cognitive dataset was recorded during an n-back task designed to assess working memory. The original protocol involved 40-s task blocks and 20-s rest blocks. To create balanced trials, the initial 20 s of each task block and the full 20-s rest blocks were used. These 20-s segments were split into 10-s trials, resulting in 108 trials per subject. The classification task for this dataset was to distinguish between the working memory task and the rest condition. b) **DSR-2C**: The Discrimination/Selection Response (DSR) dataset was collected during tasks requiring stimulus discrimination followed by response selection, which is a measure of cognitive attention. The protocol was similar to that of the N-back dataset, with 40-s task blocks and 20-s rest periods. The initial 20 s of each task block were segmented into two 10-s trials, along with the rest of the blocks, yielding a total of 72 trials per subject. Cognitive attention and rest classification were performed. c) **WG-2C**: In this dataset, participants performed word-generation (WG) and baseline (BL) tasks. During WG, subjects silently generated words starting with a given letter for 10 s, avoiding repetitions. The BL task involved relaxing and gazing at a fixation cross for 10 s. This study focused on classifying high versus low cognitive load corresponding to WG and BL, with 60 trials per participant.

2) *Preprocessing*: To ensure a fair comparison, the preprocessing pipeline for each baseline model was carefully matched to its original pretraining configuration. All EEG signals underwent band-pass filtering and 50 Hz notch filtering to remove low-frequency drifts and powerline noise. Signals were then resampled. Filter settings were specified as 0.1–75 Hz for LaBraM and 0.3–75 Hz for CBraMod. For BENDR and BIOT, which did not specify filtering, we applied a 0.5–50 Hz band-pass filter, consistent with SingLEM. Resampling rates also matched those used during the pretraining of the compared models. After filtering and resampling, the signals were scaled by a factor of 10^4 for numerical normalization. For frequency-domain features, normalization was not applied during preprocessing but was performed before training a support vector machine (SVM) classifier.

C. Evaluation Protocol

To assess generalization to unseen subjects, we employed a rigorous leave-one-subject-out cross-validation protocol for all experiments. In each fold, one subject’s entire dataset was held out as the test set, while the data from the remaining subjects were used for the training set. This training set was further split into 80% training and 20% validation, which was used for model selection and hyperparameter tuning. For all foundation models including SingLEM, we adopt a feature-extractor approach: pretrained models generated representations from the preprocessed EEG trials, which were then classified using an SVM. This protocol ensured fair and consistent comparison across models.

D. Implementation Details

We used radial basis function SVM, with hyperparameters C and γ optimized using the Optuna framework [109] on the validation split, with the objective of maximizing the macro F1-score. All experiments were implemented in Python using the scikit-learn library.

E. Evaluation Metrics

To ensure a comprehensive evaluation, we report three standard metrics: classification accuracy, macro-averaged F1-score, and Cohen’s kappa coefficient κ . Accuracy reflects the overall proportion of correctly classified samples. The macro F1-score captures the harmonic mean of precision and recall across all classes, treating each class equally and mitigating the influence of class imbalance. Cohen’s kappa coefficient quantifies the agreement between predicted and true labels beyond chance, serving as a more rigorous indicator of classification reliability.

V. RESULTS

This section presents the performance evaluation of the proposed SingLEM framework. First, we evaluate SingLEM as a multi-channel feature extractor and benchmark it against state-of-the-art foundation models and handcrafted-feature baselines. Subsequently, we employ SingLEM’s single-channel design to assess how well its learned representations align with known brain activity patterns by examining the spatial distribution of the discriminative information.

A. Comparison with State-of-the-Art Models

We evaluated SingLEM using multi-channel inputs (i.e., concatenated features from all channels) and compared its performance with baseline models across three MI and three cognitive tasks.

1) *Performance on MI Tasks*: The results for the three MI tasks are summarized in Table II. SingLEM consistently outperformed all competing foundation models and handcrafted-feature baselines across the three MI tasks.

On the **Dreyer-MI-2C** dataset, SingLEM achieved a mean accuracy of 75.27% and a macro F1-score of 75.16%, presenting a significant improvement of over 4 percentage points on both metrics when compared with the results of the next-best foundation model, CBraMod (71.10%). It also surpassed both handcrafted Fourier baselines by a margin of nearly 10 percentage points in accuracy and 12 percentage points in F1-score. For the three-class **WBCIC-MI-3C** task, SingLEM’s advantage was even more pronounced, with an accuracy of 68.26% and an F1-score of 68.17%, surpassing the second-best foundation model, CBraMod, by a substantial 8 percentage points. Notably, BENDR, BIOT, and LaBraM performed worse than the simple Fourier features, whereas SingLEM outperformed the best Fourier baseline by nearly 18 percentage points. Finally, on the large-scale **WBCIC-MI-2C** dataset, SingLEM again outperformed the comparison methods by a mean accuracy of 79.55% and an F1-score of 79.45%. This is approximately 2 percentage points higher in both metrics than the results achieved by CBraMod and over 9 percentage points higher than those of the best-performing Fourier baseline. Across all three tasks, SingLEM’s Cohen’s kappa coefficient scores achieved moderate agreement.

2) *Performance on Cognitive Tasks*: As shown in Table III, SingLEM again outperformed all baseline models across all three cognitive tasks.

On the **N-back-2C** (working memory) and **DSR-2C** (cognitive attention) tasks, SingLEM’s performance was particularly strong. It achieved 82.26% accuracy and an 81.61% F1-score on N-back, and 84.72% accuracy with an 84.50% F1-score on DSR. In both cases, Cohen’s kappa coefficient scores exceeded 0.640, indicating substantial agreement. This represents an improvement of over 4–5 percentage points in accuracy compared to the next-best foundation model, CBraMod. On the **WG-2C** (cognitive load) task, SingLEM again achieved the top performance with an accuracy of 69.87% and an F1-score of 69.58%.

B. Single-Channel Performance Analysis and Visualization

A key advantage of SingLEM is its ability to evaluate the contribution of each electrode independently, providing insights into the spatial distribution of task-relevant neural information. We analyzed the single-channel classification performance across all six datasets; the detailed numerical results are presented in Table V, and the corresponding spatial accuracy patterns are visualized as topographical maps in Fig. 2.

1) **MI Tasks:** Across all three MI datasets, discriminative activity consistently localized to regions associated with motor-related brain processes. As shown in Fig. 2, for the **Dreyer-MI-2C** dataset, the highest performance was concentrated over the right-hemisphere sensorimotor cortex, reflecting the contralateral organization of hand motor control. For the **WBCIC-MI** datasets, a similar localization to motor-related areas was observed, with top performance obtained from fronto-temporal and central sites. Interestingly, on **WBCIC-MI-2C** dataset, some posterior channels also showed above-average performance, suggesting a potential influence from non-motor cognitive processes such as visual cue processing.

2) **Cognitive Tasks:** The analysis of the three cognitive tasks revealed a distinct spatial pattern, primarily implicating the prefrontal and frontal cortex [19], [20]. For both the **N-back** (working memory) and **DSR** (cognitive attention) tasks, the highest classification accuracies were overwhelmingly concentrated in the frontal regions. The **WG-2C** (cognitive load) task showed a more distributed pattern. While frontal areas remained important, the highest accuracies were also observed over the left central-parietal and parietal regions. This is neurophysiologically consistent with the linguistic and associative processing demands of the WG task, which engages a broader network beyond just the prefrontal cortex.

Collectively, these single-channel results demonstrate that SingLEM learns spatially specific and biologically meaningful representations that reflect the unique demands of each task.

C. Ablation: Generalizability and Architectural Components

To assess the robustness of our pretraining strategy and the contribution of architectural components, we conducted two ablation studies, and the results are shown in Table IV.

First, we compared the standard SingLEM model (pretrained on a corpus excluding all downstream datasets) against a variant that included these datasets during pretraining. The results show virtually no difference between the two settings, confirming that SingLEM learns broadly transferable, domain-agnostic features without the need for prior exposure to the target domain.

Second, we evaluated the role of the feature embedding module by training a variant with this component removed. For the shorter MI tasks (4–5 s), performance degraded notably, with accuracy dropping by up to 3 percentage points (e.g., Dreyer-MI-2C). In contrast, for the longer cognitive tasks (10 s), the impact was negligible. This pattern highlights a functional interplay within the hierarchical design: the feature embedding module supplies local context by capturing short-range temporal dependencies, while the global transformer encoder alone suffices for modeling longer sequences.

These findings validate both the generalizability of SingLEM’s pretraining and the importance of its hierarchical architecture, particularly for tasks involving short trial durations.

VI. DISCUSSION

This study introduced SingLEM, a self-supervised representation learning method for single-channel EEG. The experimental results suggest four key findings: (1) SingLEM

achieves superior multi-channel performance than existing foundation models and those with handcrafted features; (2) when paired with a simple SVM, it delivers strong performance without requiring any fine-tuning; (3) its single-channel granularity enables the spatial analysis of discriminative neural activity, providing neurophysiological insights and aiding paradigm validation; and (4) it demonstrates strong generalization and robustness, with minimal reliance on task-specific data, making it suitable for diverse EEG tasks.

A. Performance and Methodological Implications

SingLEM consistently outperformed all baselines, demonstrating that pretraining on diverse single-channel EEG yields robust, generalizable features without requiring task-specific fine-tuning. Simple concatenation of single-channel features proved to be an effective “late-fusion” strategy, demonstrating that rich spatial information can be recovered even when channels are processed independently.

Dimensionality analysis revealed that higher-capacity embeddings were critical for achieving high accuracy. Low-dimensional models (BENDR: 512, BIOT: 256, and LaBraM: 200) were computationally efficient but consistently underperformed, whereas the top-performing models SingLEM (e.g., 2,592 for Dreyer-MI-2C) and CBraMod (e.g., 19,000 for Dreyer-MI-2C) utilized substantially richer spaces. SingLEM achieved state-of-the-art performance without requiring CBraMod’s extreme dimensionality, balancing between representation capacity and efficiency. Importantly, the relatively weak out-of-the-box performance of some foundation models such as BENDR, BIOT, and LaBraM, does not imply they are suboptimal; rather, it reflects their design-intended reliance on full fine-tuning on each downstream task. In contrast, SingLEM is effective as a “ready-to-use” feature extractor, reducing computational and data demands while maintaining high performance.

The ablation results further support these conclusions. Pretraining was shown to produce domain-agnostic representations that generalized well even without exposure to task-specific data. Moreover, the feature embedding module contributed significantly to performance on short-term trial tasks, whereas its effect diminished for longer sequences. This indicates a functional complementarity within the hierarchical design, where local embedding enriches short-term dependencies and the global encoder handles extended temporal dynamics.

B. Neurophysiological Plausibility and Paradigm Evaluation

The single-channel analysis in this study not only quantified the performance of SingLEM but also provided a means of scientific validation, demonstrating that SingLEM extracts neurophysiologically meaningful features rather than task-irrelevant cues within the data. This was consistently observed across both motor and cognitive domains.

For the MI tasks, the high-performing channels localized to the sensorimotor cortex, including the central, fronto-central, and fronto-temporal regions, which are well established as regions of motor planning and execution. The lateralized

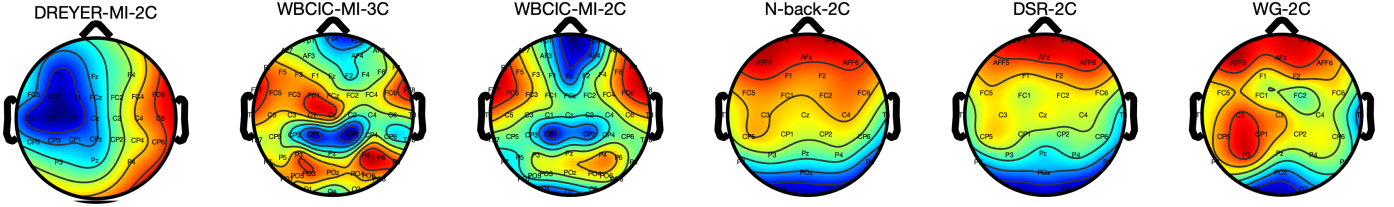


Fig. 2. Topographical accuracy maps for the Dreyer-MI-2C, WBCIC-MI-3C, WBCIC-MI-2C, N-back-2C, DSR-2C, and WG-2C datasets. Note: accuracy values were min-max normalized (per map) for visualization clarity.

TABLE II

CLASSIFICATION RESULTS ON THREE MI DATASETS. THE BEST RESULTS FOR EACH METRIC AND DATASET ARE HIGHLIGHTED IN BOLD

Models	Dreyer-MI-2C			WBCIC-MI-3C			WBCIC-MI-2C		
	Accuracy	F1-score	Cohen's κ	Accuracy	F1-score	Cohen's κ	Accuracy	F1-score	Cohen's κ
BENDR	50.51 \pm 05.04	50.24 \pm 05.07	0.010 \pm 0.100	35.28 \pm 02.78	34.84 \pm 02.88	0.029 \pm 0.041	51.32 \pm 03.13	51.24 \pm 03.17	0.026 \pm 0.062
BIOT	56.85 \pm 08.15	52.64 \pm 10.55	0.136 \pm 0.153	37.04 \pm 04.58	33.78 \pm 05.27	0.055 \pm 0.068	51.20 \pm 04.12	48.25 \pm 05.32	0.023 \pm 0.082
LaBraM	49.91 \pm 00.22	34.02 \pm 03.02	0.001 \pm 0.001	40.04 \pm 04.69	37.17 \pm 05.30	0.100 \pm 0.070	56.88 \pm 06.04	56.15 \pm 06.18	0.137 \pm 0.120
CBraMod	71.10 \pm 08.33	70.62 \pm 08.90	0.422 \pm 0.166	59.93 \pm 09.77	58.96 \pm 09.96	0.398 \pm 0.146	77.56 \pm 12.22	77.26 \pm 12.62	0.551 \pm 0.244
Fourier ($k = 8$)	65.36 \pm 07.70	64.98 \pm 07.97	0.307 \pm 0.154	50.41 \pm 06.16	48.33 \pm 08.14	0.256 \pm 0.092	70.07 \pm 10.12	69.76 \pm 10.30	0.401 \pm 0.202
Fourier ($k = 16$)	64.67 \pm 08.64	63.37 \pm 10.47	0.293 \pm 0.172	48.38 \pm 06.76	44.88 \pm 09.57	0.225 \pm 0.101	70.25 \pm 10.34	69.86 \pm 10.77	0.708 \pm 0.103
SingLEM (ours)	75.27 \pm 08.28	75.16 \pm 08.32	0.505 \pm 0.165	68.26 \pm 12.13	68.17 \pm 12.20	0.523 \pm 0.181	79.55 \pm 13.68	79.45 \pm 13.76	0.590 \pm 0.273

TABLE III

CLASSIFICATION RESULTS ON THREE COGNITIVE TASK DATASETS. THE BEST RESULTS FOR EACH METRIC AND DATASET ARE HIGHLIGHTED IN BOLD

Models	N-back-2C			DSR-2C			WG-2C		
	Accuracy	F1-score	Cohen's κ	Accuracy	F1-score	Cohen's κ	Accuracy	F1-score	Cohen's κ
BENDR	52.96 \pm 05.76	52.75 \pm 05.71	0.059 \pm 0.115	54.59 \pm 06.40	54.43 \pm 06.44	0.091 \pm 0.127	52.24 \pm 05.90	51.94 \pm 06.03	0.044 \pm 0.118
BIOT	58.90 \pm 09.08	54.66 \pm 12.07	0.178 \pm 0.181	60.84 \pm 09.53	57.91 \pm 11.58	0.216 \pm 0.190	56.67 \pm 06.13	52.54 \pm 08.86	0.133 \pm 0.122
LaBraM	62.25 \pm 07.97	59.84 \pm 10.73	0.245 \pm 0.159	66.83 \pm 12.06	65.60 \pm 13.21	0.336 \pm 0.241	60.64 \pm 08.99	56.44 \pm 12.48	0.212 \pm 0.179
CBraMod	78.13 \pm 09.58	76.81 \pm 11.89	0.562 \pm 0.191	79.59 \pm 09.55	78.81 \pm 10.47	0.591 \pm 0.191	69.36 \pm 08.28	67.93 \pm 09.53	0.387 \pm 0.165
Fourier ($k = 8$)	70.19 \pm 10.14	68.73 \pm 11.36	0.403 \pm 0.202	72.60 \pm 10.27	71.11 \pm 12.48	0.451 \pm 0.205	61.54 \pm 06.90	58.31 \pm 10.04	0.230 \pm 0.138
Fourier ($k = 16$)	72.22 \pm 09.96	70.52 \pm 12.18	0.444 \pm 0.199	75.75 \pm 10.59	74.39 \pm 13.00	0.515 \pm 0.211	62.56 \pm 10.10	58.75 \pm 13.37	0.251 \pm 0.202
SingLEM (ours)	82.34 \pm 09.73	81.65 \pm 11.90	0.646 \pm 0.194	84.72 \pm 09.35	84.50 \pm 09.76	0.694 \pm 0.187	69.87 \pm 07.41	69.58 \pm 07.58	0.397 \pm 0.148

TABLE IV

ABLATION STUDY ON THE PRETRAINING STRATEGY AND ARCHITECTURAL COMPONENTS. RESULTS ARE REPORTED FOR: (1) THE STANDARD SINGLEM MODEL PRETRAINED WITHOUT TASK-SPECIFIC DATA, (2) A VARIANT PRETRAINED ON DATA INCLUDING TASK-SPECIFIC DATA, AND (3) A VARIANT WITH THE FEATURE EMBEDDING MODULE REMOVED. PERFORMANCE METRICS ARE SHOWN ACROSS SIX DOWNSTREAM TASKS

Metric	Dreyer-2C	WBCIC-3C	WBCIC-2C	N-back-2C	DSR-2C	WG-2C
Standard SingLEM (Out-of-Distribution)						
Accuracy	75.27	68.26	79.55	82.34	84.72	69.87
F1-score	75.16	68.17	79.45	81.65	84.50	69.58
Cohen's κ	0.505	0.523	0.590	0.646	0.694	0.397
Pretrained with Task-specific Data (In-Distribution)						
Accuracy	75.33	68.29	79.10	82.51	84.83	69.68
F1-score	75.21	68.13	79.00	81.83	84.55	69.43
Cohen's κ	0.506	0.524	0.581	0.650	0.696	0.393
Ablated (No Feature Embedding Module)						
Accuracy	72.56	66.17	78.04	82.09	84.62	69.04
F1-score	72.40	66.02	77.94	81.39	84.22	68.74
Cohen's κ	0.451	0.492	0.560	0.641	0.692	0.380

responses observed in the results for the Dreyer-MI dataset further aligned with the contralateral organization of the motor system, underscoring the biological validity of the learned features.

For cognitive tasks, discriminative patterns shifted in ac-

cordance with task demands. In N-back (working memory) and DSR (attention) tasks, performance was dominated by the frontal electrodes (FP1, FP2), reflecting the role of the prefrontal cortex in attention-related processes [19], [20]. The results for the WG task showed a broader distribution, with high performance in the frontal regions across cognitive tasks, as well as involvement of the left central-parietal areas. This distinct activation suggests that SingLEM captured task-specific neural activity associated with linguistic and associative processes beyond those for general executive control.

Importantly, this granularity also enabled the evaluation of experimental paradigms. In the WBCIC-MI-2C data, unexpectedly high performance was observed in occipital and parietal regions, likely reflecting visual cue processing rather than MI alone. Such findings demonstrate the ability of SingLEM to detect potential confounds and the advantages of its interpretability over less transparent multi-channel models.

C. Limitations and Future Work

While this study demonstrates the significant potential of a single-channel foundation model, it also opens several important avenues for future research. 1) Advanced spatial fusion: Our late-fusion strategy, which concatenates channel represen-

tations, was effective but does not explicitly capture spatial relationships. Future work should explore more advanced spatial fusion methods. 2) Reference electrode invariance: SingLEM is hardware-independent with respect to channel layout, but like most EEG models, its representations remain sensitive to the choice of reference electrodes. This can limit comparability across datasets recorded with different referencing schemes. Developing methods for learning reference-invariant representations is, therefore, a crucial next step. 3) Domain adaptation and continual learning: Beyond its use as a “frozen” feature extractor, future work should explore SingLEM’s adaptability in two key directions. First, its potential for cross-modality transfer should be assessed by fine-tuning the model on other physiological signals (e.g., electrocardiogram, electromyography, or electrocorticography). Second, continual pretraining strategies should be developed to allow the model to update its core knowledge as new large-scale EEG datasets become available. These directions could further enhance SingLEM’s versatility and broaden its practical impact.

VII. CONCLUSION

This study introduced SingLEM, a foundation model designed to overcome the hardware dependency of existing EEG models by learning representations at the single-channel level. By pretraining on a diverse corpus of 71 public datasets consisting of over 10,200 multi-channel hours (the equivalent of over 357,000 single-channel hours), SingLEM learns features that are both robust and hardware agnostic. This was validated through extensive evaluations across six downstream tasks, where SingLEM consistently outperformed all the comparison multi-channel foundation models in this study.

From these results, we draw several key conclusions. First, SingLEM successfully extracts rich, generalizable representations from individual EEG channels, which are highly effective for diverse downstream tasks. Second, its design as a fixed feature extractor, paired with a lightweight SVM classifier, provides a resource-efficient solution that delivers state-of-the-art performance without the need for computationally expensive fine-tuning. Third, SingLEM’s single-channel granularity serves as a useful analytical tool, enabling more detailed and interpretable analysis of brain function by isolating the contribution of each electrode. Finally, by decoupling feature learning from rigid hardware configurations, SingLEM offers a practical solution to the challenge of montage dependency in EEG research.

ACKNOWLEDGMENT

We would like to thank Editage (www.editage.jp) for English language editing.

REFERENCES

- [1] H. Yuan *et al.*, “Brain–computer interfaces using sensorimotor rhythms: Current state and future perspectives,” *IEEE Trans. Biomed. Eng.*, vol. 61, no. 5, pp. 1425–1435, 2014.
- [2] A. Supratak *et al.*, “DeepSleepNet: A model for automatic sleep stage scoring based on raw single-channel EEG,” *IEEE Trans. Neural Syst. Rehabil. Eng.*, vol. 25, no. 11, pp. 1998–2008, 2017.
- [3] T. Shoji *et al.*, “Automated detection of abnormalities from an EEG recording of epilepsy patients with a compact convolutional neural network,” *Biomed. Signal Process. Control*, vol. 70, p. 103013, 2021.
- [4] X. Wang *et al.*, “EEG-based seizure onset detection of frontal and temporal lobe epilepsies using 1DCNN,” *IEEE Trans. Neural Syst. Rehabil. Eng.*, vol. 33, pp. 2263–2272, 2025.
- [5] K. Meng *et al.*, “Real-time epileptic seizure prediction method with spatio-temporal information transfer learning,” *IEEE J. Biomed. Health Inform.*, vol. 29, no. 3, pp. 2222–2232, 2025.
- [6] M. Emad-Ud-Din *et al.*, “Electroencephalography machine-learning features and methods for early diagnosis and classification of Parkinson’s disease (2013–2023): A review,” *IEEE Sensors J.*, vol. 25, no. 12, pp. 21 017–21 032, 2025.
- [7] A. Othmani *et al.*, “Machine-learning-based approaches for post-traumatic stress disorder diagnosis using video and EEG sensors: A review,” *IEEE Sensors J.*, vol. 23, no. 20, pp. 24 135–24 151, 2023.
- [8] S. M. Alarcão *et al.*, “Emotions recognition using EEG signals: A survey,” *IEEE Trans. Affect. Comput.*, vol. 10, no. 3, pp. 374–393, 2019.
- [9] Y. Ding *et al.*, “EmT: A novel transformer for generalized cross-subject EEG emotion recognition,” *IEEE Trans. Neural Netw. Learn. Syst.*, vol. 36, no. 6, pp. 10 381–10 393, 2025.
- [10] W. Wang *et al.*, “EEG-based cross-subject emotion recognition using sparse Bayesian learning with enhanced covariance alignment,” *IEEE Trans. Affect. Comput.*, vol. 16, no. 2, pp. 1190–1204, 2025.
- [11] F. Lotte *et al.*, “A review of classification algorithms for EEG-based brain–computer interfaces: a 10 year update,” *J. Neural Eng.*, vol. 15, no. 3, p. 031005, 2018.
- [12] Y. Roy *et al.*, “Deep learning-based electroencephalography analysis: a systematic review,” *J. Neural Eng.*, vol. 16, no. 5, p. 051001, 2019.
- [13] P. Chen *et al.*, “Unsupervised domain adaptation with synchronized self-training for cross-domain motor imagery recognition,” *IEEE J. Biomed. Health Inform.*, vol. 29, no. 5, pp. 3664–3677, 2025.
- [14] G. Liu *et al.*, “Fine-grained spatial-frequency-time framework for motor imagery brain–computer interface,” *IEEE J. Biomed. Health Inform.*, vol. 29, no. 6, pp. 4121–4133, 2025.
- [15] X. He *et al.*, “Leveraging peripheral visual stimuli for enhanced SSVEP-based BCIs in fast calibration scenario,” *IEEE Sensors J.*, vol. 25, no. 10, pp. 17 683–17 695, 2025.
- [16] J. Chen *et al.*, “A transformer-based deep neural network model for SSVEP classification,” *Neural Netw.*, vol. 164, pp. 521–534, 2023.
- [17] C. Wan *et al.*, “Advancing sleep disorder diagnostics: A transformer-based EEG model for sleep stage classification and OSA prediction,” *IEEE J. Biomed. Health Inform.*, vol. 29, no. 2, pp. 878–886, 2025.
- [18] A. Ito *et al.*, “SleepSatelightFTC: A lightweight and interpretable deep learning model for single-channel EEG-based sleep stage classification,” *IEEE Access*, vol. 13, pp. 46 263–46 272, 2025.
- [19] Y.-K. Hong *et al.*, “Characteristics of physical environments that enhance learning: A systematic review of EEG-based empirical studies,” *J. Environ. Psychol.*, vol. 102, p. 102525, 2025.
- [20] Y. Zhou *et al.*, “Enhanced cognitive load detection in air traffic control operators using EEG and a hybrid deep learning approach,” *IEEE Access*, vol. 13, pp. 12 127–12 137, 2025.
- [21] J. Devlin *et al.*, “BERT: Pre-training of deep bidirectional transformers for language understanding,” in *Proc. Conf. North Amer. Chapter Assoc. Comput. Linguistics (NAACL-HLT)*, 2019, pp. 4171–4186.
- [22] J. Achiam *et al.*, “GPT-4 technical report,” *arXiv preprint arXiv:2303.08774*, 2023.
- [23] A. Dosovitskiy *et al.*, “An image is worth 16x16 words: Transformers for image recognition at scale,” *arXiv preprint arXiv:2010.11929*, 2020.
- [24] J. Qiu *et al.*, “Large AI models in health informatics: Applications, challenges, and the future,” *IEEE J. Biomed. Health Inform.*, vol. 27, no. 12, pp. 6074–6087, 2023.
- [25] Y. He *et al.*, “Foundation model for advancing healthcare: Challenges, opportunities and future directions,” *IEEE Rev. Biomed. Eng.*, vol. 18, pp. 172–191, 2025.
- [26] W. Khan *et al.*, “A comprehensive survey of foundation models in medicine,” *IEEE Rev. Biomed. Eng.*, pp. 1–22, 2025.
- [27] D. Kostas *et al.*, “BENDR: Using transformers and a contrastive self-supervised learning task to learn from massive amounts of EEG data,” *Front. Hum. Neurosci.*, vol. 15, p. 653659, 2021.
- [28] C. Yang *et al.*, “Biot: Biosignal transformer for cross-data learning in the wild,” *Proc. Adv. Neural Inf. Process. Syst. (NeurIPS)*, vol. 36, pp. 78 240–78 260, 2023.
- [29] W. Jiang *et al.*, “Large brain model for learning generic representations with tremendous EEG data in BCI,” in *Proc. Int. Conf. Learn.*

TABLE V

ACCURACY RESULTS FOR INDIVIDUAL CHANNELS ACROSS THE FOLLOWING SIX DATASETS: DREYER-MI-2C (D1), WBCIC-MI-3C (D2), WBCIC-MI-2C (D3), N-BACK-2C (D4), DSR-2C (D5), AND WG-2C (D6). A DASH (–) INDICATES THAT THE CHANNEL WAS NOT PRESENT IN THE RESPECTIVE DATASET

Ch.	D1	D2	D3	D4	D5	D6	Ch.	D1	D2	D3	D4	D5	D6	Ch.	D1	D2	D3	D4	D5	D6
Fpz	–	42.95	57.58	–	–	–	FC2	57.62	49.32	64.60	77.56	77.30	59.10	CP5	54.79	49.23	64.59	76.50	77.72	62.88
Fp1	–	47.26	62.96	82.23	83.17	64.04	FC3	50.57	51.50	67.45	–	–	–	CP6	61.58	45.83	64.55	72.36	74.52	60.32
Fp2	–	42.71	60.04	82.37	82.80	64.42	FC4	60.42	49.10	66.68	–	–	–	TP7	–	48.50	64.38	–	–	–
AFz	–	–	80.31	81.94	63.78	–	FC5	54.32	51.95	69.81	77.60	78.04	61.41	TP8	–	46.01	64.92	–	–	–
AF3	–	47.62	63.67	–	–	–	FC6	62.89	51.89	69.72	77.49	77.35	61.03	Pz	55.45	46.80	66.15	71.55	72.38	60.00
AF4	–	46.41	61.08	–	–	–	FT7	–	54.07	71.32	–	–	–	P3	56.40	52.26	65.84	72.86	74.57	64.04
AF7	–	48.35	66.60	–	–	–	FT8	–	54.25	71.19	–	–	–	P4	60.51	54.47	68.11	72.08	73.93	60.45
AF8	–	48.01	67.39	–	–	–	Cz	54.02	53.26	63.99	75.43	77.46	61.99	P5	–	49.32	63.64	–	–	–
AFF5	–	–	82.02	80.61	64.62	–	C1	50.51	52.50	64.44	–	–	–	P6	–	53.80	67.03	–	–	–
AFF6	–	–	–	80.20	82.11	62.82	C2	57.89	46.89	63.69	–	–	–	P7	–	50.75	62.71	69.16	70.83	61.47
Fz	55.12	48.14	59.77	–	–	–	C3	50.24	50.26	65.25	76.67	77.62	63.72	P8	–	52.71	64.37	64.92	68.75	58.91
F1	–	49.59	63.61	78.49	78.10	60.90	C4	60.92	47.68	64.45	77.21	76.50	60.51	POz	–	51.56	66.48	67.06	70.83	56.73
F2	–	45.74	64.09	78.10	79.33	62.44	C5	51.28	50.68	66.91	–	–	–	PO3	–	52.77	65.29	–	–	–
F3	51.34	50.83	66.42	–	–	–	C6	62.77	48.53	66.97	–	–	–	PO4	–	50.95	67.20	–	–	–
F4	58.45	47.29	65.97	–	–	–	T7	–	52.74	68.75	74.04	73.72	60.71	PO5	–	51.11	64.30	–	–	–
F5	–	51.53	68.27	–	–	–	T8	–	49.71	68.07	70.58	71.79	56.09	PO6	–	51.53	66.84	–	–	–
F6	–	48.04	69.00	–	–	–	CPz	53.99	–	–	–	–	–	PO7	–	51.41	63.00	–	–	–
F7	–	51.89	70.18	–	–	–	CP1	53.75	41.13	58.62	74.75	75.91	63.01	PO8	–	50.35	65.28	–	–	–
F8	–	50.41	70.72	–	–	–	CP2	57.44	39.86	60.20	74.50	75.16	61.03	Oz	–	46.47	60.98	–	–	–
FCz	54.41	50.08	63.36	–	–	–	CP3	53.39	45.26	63.17	–	–	–	O1	–	49.29	60.53	62.54	66.56	55.19
FC1	51.67	52.99	65.39	76.82	76.01	60.58	CP4	59.40	48.26	63.85	–	–	–	O2	–	49.80	63.33	63.21	66.51	56.28

Represent. (ICLR), 2024. [Online]. Available: <https://openreview.net/forum?id=QzTpTRVtrP>

[30] J. Wang *et al.*, “CBraMod: A criss-cross brain foundation model for EEG decoding,” in *Proc. Int. Conf. Learn. Represent. (ICLR)*, 2025. [Online]. Available: <https://openreview.net/forum?id=NPNUHgHF2w>

[31] K. He *et al.*, “Masked autoencoders are scalable vision learners,” in *Proc. IEEE/CVF Conf. Comput. Vis. Pattern Recognit. (CVPR)*, 2022, pp. 16 000–16 009.

[32] R. T. Schirrmeister *et al.*, “Deep learning with convolutional neural networks for EEG decoding and visualization,” *Hum. Brain Mapp.*, vol. 38, no. 11, pp. 5391–5420, 2017.

[33] V. J. Lawhern *et al.*, “EEGNet: a compact convolutional neural network for EEG-based brain–computer interfaces,” *J. Neural Eng.*, vol. 15, no. 5, p. 056013, 2018.

[34] J. Jing *et al.*, “Development of expert-level classification of seizures and rhythmic and periodic patterns during EEG interpretation,” *Neurology*, vol. 100, no. 17, pp. e1750–e1762, 2023.

[35] Y. Song *et al.*, “EEG conformer: Convolutional transformer for EEG decoding and visualization,” *IEEE Trans. Neural Syst. Rehabil. Eng.*, vol. 31, pp. 710–719, 2023.

[36] Y. Ding *et al.*, “EEG-deformer: A dense convolutional transformer for brain–computer interfaces,” *IEEE J. Biomed. Health Inform.*, vol. 29, no. 3, pp. 1909–1918, 2025.

[37] Y. Roy *et al.*, “Deep learning-based electroencephalography analysis: a systematic review,” *J. Neural Eng.*, vol. 16, no. 5, p. 051001, 2019.

[38] H. Cho *et al.*, “EEG datasets for motor imagery brain–computer interface,” *GigaScience*, vol. 6, no. 7, p. gix034, 2017.

[39] G. Schalk *et al.*, “BCI2000: a general-purpose brain-computer interface (BCI) system,” *IEEE Trans. Biomed. Eng.*, vol. 51, no. 6, pp. 1034–1043, 2004.

[40] J. Shin *et al.*, “Open access dataset for EEG+NIRS single-trial classification,” *IEEE Trans. Neural Syst. Rehabil. Eng.*, vol. 25, no. 10, pp. 1735–1745, 2017.

[41] M. Kaya *et al.*, “A large electroencephalographic motor imagery dataset for electroencephalographic brain computer interfaces,” *Sci. Data*, vol. 5, no. 1, pp. 1–16, 2018.

[42] M.-H. Lee *et al.*, “EEG dataset and OpenBMI toolbox for three BCI paradigms: An investigation into BCI illiteracy,” *GigaScience*, vol. 8, no. 5, p. giz002, 2019.

[43] S. Brandl *et al.*, “Motor imagery under distraction—an open access BCI dataset,” *Front. Neurosci.*, vol. 14, p. 566147, 2020.

[44] Z. Chen *et al.*, “Open access dataset integrating EEG and fNIRS during Stroop tasks,” *Sci. Data*, vol. 10, no. 1, p. 618, 2023.

[45] X. Mou *et al.*, “ChineseEEG: A Chinese linguistic corpora EEG dataset for semantic alignment and neural decoding,” *Sci. Data*, vol. 11, no. 1, p. 550, 2024.

[46] S. Getzmann *et al.*, “Resting-state EEG data before and after cognitive activity across the adult lifespan and a 5-year follow-up,” *Sci. Data*, vol. 11, no. 1, p. 988, 2024.

[47] X. Ji *et al.*, “EEG and fNIRS datasets based on Stroop task during two weeks of high-altitude exposure in new immigrants,” *Sci. Data*, vol. 11, no. 1, p. 350, 2024.

[48] M. Momenian *et al.*, “Le petit prince hong kong (lpphk): Naturalistic fMRI and EEG data from older Cantonese speakers,” *Sci. Data*, vol. 11, no. 1, p. 992, 2024.

[49] C. Xiang *et al.*, “A resting-state EEG dataset for sleep deprivation,” *Sci. Data*, vol. 11, no. 1, p. 427, 2024.

[50] A. Babayan *et al.*, “A mind-brain-body dataset of MRI, EEG, cognition, emotion, and peripheral physiology in young and old adults,” *Sci. Data*, vol. 6, no. 1, pp. 1–21, 2019.

[51] H. van Dijk *et al.*, “The two decades brainclinics research archive for insights in neurophysiology (TDBRAIN) database,” *Sci. Data*, vol. 9, no. 1, p. 333, 2022.

[52] T. D. Ngo *et al.*, “An EEG & eye-tracking dataset of ALS patients & healthy people during eye-tracking-based spelling system usage,” *Sci. Data*, vol. 11, no. 1, p. 664, 2024.

[53] T. Grootswagers *et al.*, “Human EEG recordings for 1,854 concepts presented in rapid serial visual presentation streams,” *Sci. Data*, vol. 9, no. 1, p. 3, 2022.

[54] P. Dzianok *et al.*, “PEARL-Neuro database: EEG, fMRI, health and lifestyle data of middle-aged people at risk of dementia,” *Sci. Data*, vol. 11, no. 1, p. 276, 2024.

[55] J. Ma *et al.*, “A large EEG dataset for studying cross-session variability in motor imagery brain–computer interface,” *Sci. Data*, vol. 9, no. 1, p. 531, 2022.

[56] Y. Chen *et al.*, “An EEG dataset of neural signatures in a competitive two-player game encouraging deceptive behavior,” *Sci. Data*, vol. 11, no. 1, p. 389, 2024.

[57] Z. Cao *et al.*, “Multi-channel EEG recordings during a sustained-attention driving task,” *Sci. Data*, vol. 6, no. 1, p. 19, 2019.

[58] Q. K. Telesford *et al.*, “An open-access dataset of naturalistic viewing using simultaneous EEG-fMRI,” *Sci. Data*, vol. 10, no. 1, p. 554, 2023.

[59] X. Ma *et al.*, “Multi-channel EEG recording during motor imagery of different joints from the same limb,” *Sci. Data*, vol. 7, no. 1, p. 191, 2020.

[60] B. Yang *et al.*, “A multi-day and high-quality EEG dataset for motor imagery brain–computer interface,” *Sci. Data*, vol. 12, no. 1, p. 488, 2025.

[61] K. Chen *et al.*, “A resource for assessing dynamic binary choices in the adult brain using EEG and mouse-tracking,” *Sci. Data*, vol. 9, no. 1, p. 416, 2022.

[62] P. Dreyer *et al.*, “A large EEG database with users’ profile information for motor imagery brain–computer interface research,” *Sci. Data*, vol. 10, no. 1, p. 580, 2023.

[63] Y. Wang *et al.*, “A test-retest resting, and cognitive state EEG dataset during multiple subject-driven states,” *Sci. Data*, vol. 9, no. 1, p. 566, 2022.

[64] J. Chen *et al.*, “A large finer-grained affective computing EEG dataset,” *Sci. Data*, vol. 10, no. 1, p. 740, 2023.

[65] J. Shin *et al.*, “Simultaneous acquisition of EEG and NIRS during cognitive tasks for an open access dataset,” *Sci. Data*, vol. 5, no. 1, pp. 1–16, 2018.

[66] M. F. Hinss *et al.*, “Open multi-session and multi-task EEG cognitive dataset for passive brain-computer interface applications,” *Sci. Data*, vol. 10, no. 1, p. 85, 2023.

[67] N. Gebodh *et al.*, “Dataset of concurrent EEG, ECG, and behavior with multiple doses of transcranial electrical stimulation,” *Sci. Data*, vol. 8, no. 1, p. 274, 2021.

[68] N. Nieto *et al.*, “Thinking out loud, an open-access EEG-based BCI dataset for inner speech recognition,” *Sci. Data*, vol. 9, no. 1, p. 52, 2022.

[69] K. Won *et al.*, “EEG dataset for RSVP and P300 speller brain-computer interfaces,” *Sci. Data*, vol. 9, no. 1, p. 388, 2022.

[70] N. Hollenstein *et al.*, “ZuCo, a simultaneous EEG and eye-tracking resource for natural sentence reading,” *Sci. Data*, vol. 5, no. 1, pp. 1–13, 2018.

[71] Y. Liu *et al.*, “Lower limb motor imagery EEG dataset based on the multi-paradigm and longitudinal-training of stroke patients,” *Sci. Data*, vol. 12, no. 1, p. 314, 2025.

[72] J. Wagner *et al.*, “High-density EEG mobile brain/body imaging data recorded during a challenging auditory gait pacing task,” *Sci. Data*, vol. 6, no. 1, p. 211, 2019.

[73] R. Ghosh *et al.*, “SAM 40: Dataset of 40 subject EEG recordings to monitor the induced-stress while performing Stroop color-word test, arithmetic task, and mirror image recognition task,” *Data Brief*, vol. 40, p. 107772, 2022.

[74] P. A. Valdes-Sosa *et al.*, “The Cuban Human Brain Mapping Project, a young and middle age population-based EEG, MRI, and cognition dataset,” *Sci. Data*, vol. 8, no. 1, p. 45, 2021.

[75] A. Mheich *et al.*, “HD-EEG for tracking sub-second brain dynamics during cognitive tasks,” *Sci. Data*, vol. 8, no. 1, p. 32, 2021.

[76] H. Liu *et al.*, “An EEG motor imagery dataset for brain computer interface in acute stroke patients,” *Sci. Data*, vol. 11, no. 1, p. 131, 2024.

[77] G.-Y. Choi *et al.*, “EEG dataset for the recognition of different emotions induced in voice-user interaction,” *Sci. Data*, vol. 11, no. 1, p. 1084, 2024.

[78] X. Wei *et al.*, “ANPHY-Sleep: an open sleep database from healthy adults using high-density scalp electroencephalogram,” *Sci. Data*, vol. 11, no. 1, p. 896, 2024.

[79] M. Gu *et al.*, “An open dataset for human SSVEPs in the frequency range of 1–60 Hz,” *Sci. Data*, vol. 11, no. 1, p. 196, 2024.

[80] W. Mumtaz *et al.*, “A wavelet-based technique to predict treatment outcome for major depressive disorder,” *PLoS ONE*, vol. 12, no. 2, p. e0171409, 2017.

[81] S. Iwama *et al.*, “High-density scalp electroencephalogram dataset during sensorimotor rhythm-based brain-computer interfacing,” *Sci. Data*, vol. 10, no. 1, p. 385, 2023.

[82] F. Simistira Liwicki *et al.*, “Bimodal electroencephalography-functional magnetic resonance imaging dataset for inner-speech recognition,” *Sci. Data*, vol. 10, no. 1, p. 378, 2023.

[83] A. H. Moffa *et al.*, “Neuromodulatory effects of theta burst stimulation to the prefrontal cortex,” *Sci. Data*, vol. 9, no. 1, p. 717, 2022.

[84] A. R. Cuevas-Romero *et al.*, “An electroencephalography-based database for studying the effects of acoustic therapies for tinnitus treatment,” *Sci. Data*, vol. 9, no. 1, p. 500, 2022.

[85] X. Pei *et al.*, “A simultaneous electroencephalography and eye-tracking dataset in elite athletes during alertness and concentration tasks,” *Sci. Data*, vol. 9, no. 1, p. 465, 2022.

[86] N. Lin *et al.*, “An EEG dataset for interictal epileptiform discharge with spatial distribution information,” *Sci. Data*, vol. 12, no. 1, p. 229, 2025.

[87] Y. G. Pavlov *et al.*, “Pupillometry and electroencephalography in the digit span task,” *Sci. Data*, vol. 9, no. 1, p. 325, 2022.

[88] B. Liu *et al.*, “eldbeta: A large eldercare-oriented benchmark database of SSVEP-BCI for the aging population,” *Sci. Data*, vol. 9, no. 1, p. 252, 2022.

[89] H. Cai *et al.*, “A multi-modal open dataset for mental-disorder analysis,” *Sci. Data*, vol. 9, no. 1, p. 178, 2022.

[90] D. Pascucci *et al.*, “Source imaging of high-density visual evoked potentials with multi-scale brain parcellations and connectomes,” *Sci. Data*, vol. 9, no. 1, p. 9, 2022.

[91] J. R. Stieger *et al.*, “Continuous sensorimotor rhythm based brain computer interface learning in a large population,” *Sci. Data*, vol. 8, no. 1, p. 98, 2021.

[92] S. Lopez *et al.*, “Automated identification of abnormal adult EEGs,” in *Proc. IEEE Signal Process. Med. Biol. Symp. (SPMB)*, 2015, pp. 1–5.

[93] G. Buckwalter *et al.*, “Recent advances in the TUH EEG corpus: improving the interrater agreement for artifacts and epileptiform events,” in *Proc. IEEE Signal Process. Med. Biol. Symp. (SPMB)*, 2021, pp. 1–3.

[94] L. Veloso *et al.*, “Big data resources for EEGs: Enabling deep learning research,” in *Proc. IEEE Signal Process. Med. Biol. Symp. (SPMB)*, 2017, pp. 1–3.

[95] A. Harati *et al.*, “Improved EEG event classification using differential energy,” in *Proc. IEEE Signal Process. Med. Biol. Symp. (SPMB)*, 2015, pp. 1–4.

[96] V. Shah *et al.*, “The temple university hospital seizure detection corpus,” *Front. Neuroinform.*, vol. 12, p. 83, 2018.

[97] E. von Weltin *et al.*, “Electroencephalographic slowing: A primary source of error in automatic seizure detection,” in *Proc. IEEE Signal Process. Med. Biol. Symp. (SPMB)*, 2017, pp. 1–5.

[98] T. Grootswagers *et al.*, “Human infant EEG recordings for 200 object images presented in rapid visual streams,” *Sci. Data*, vol. 12, no. 1, p. 407, 2025.

[99] W. Yi *et al.*, “A multi-modal dataset of electroencephalography and functional near-infrared spectroscopy recordings for motor imagery of multi-types of joints from unilateral upper limb,” *Sci. Data*, vol. 12, no. 1, pp. 1–11, 2025.

[100] M. Rybář *et al.*, “Simultaneous EEG and fNIRS recordings for semantic decoding of imagined animals and tools,” *Sci. Data*, vol. 12, no. 1, p. 613, 2025.

[101] B. He *et al.*, “A simultaneous EEG and eye-tracking dataset for remote sensing object detection,” *Sci. Data*, vol. 12, no. 1, p. 651, 2025.

[102] S. Xue *et al.*, “A multi-subject and multi-session EEG dataset for modelling human visual object recognition,” *Sci. Data*, vol. 12, no. 1, p. 663, 2025.

[103] Y. Bai *et al.*, “TMNRED, a Chinese language EEG dataset for fuzzy semantic target identification in natural reading environments,” *Sci. Data*, vol. 12, no. 1, p. 701, 2025.

[104] J. P. C. Moreira *et al.*, “An open-access EEG dataset for speech decoding: Exploring the role of articulation and coarticulation,” *Sci. Data*, vol. 12, no. 1, pp. 1–15, 2025.

[105] Q. Wang *et al.*, “Le Petit Prince (LPP) multi-talker: Naturalistic 7 T fMRI and EEG dataset,” *Sci. Data*, vol. 12, no. 1, pp. 1–11, 2025.

[106] G. Zhang *et al.*, “A large-scale MEG and EEG dataset for object recognition in naturalistic scenes,” *Sci. Data*, vol. 12, no. 1, pp. 1–10, 2025.

[107] X. Tao *et al.*, “A multimodal physiological dataset for driving behaviour analysis,” *Sci. Data*, vol. 11, no. 1, p. 378, 2024.

[108] E. López-Larraz *et al.*, “Bitbrain open access sleep dataset,” 2025.

[109] T. Akiba *et al.*, “Optuna: A next-generation hyperparameter optimization framework,” in *Proc. 25th ACM SIGKDD Int. Conf. Knowl. Discovery Data Mining*, 2019.